ACS APPLIED ENGINEERING MATERIALS

pubs.acs.org/acsaenm Article

Tailoring Polyamide Nanocomposites: The Synergistic Effects of SWCNT Chirality and Maleic Anhydride Grafting

Mehedi Hasan, Khayrul Islam, and A. K. M. Masud*

Cite This: ACS Appl. Eng. Mater. 2024, 2, 1593−1602 Read Online

ACCESS | Metrics & More | Article Recommendations

ABSTRACT: In the realm of advanced material science, polymer nanocomposites augmented with carbon nanotubes (CNTs) have accumulated significant attention due to their potential to markedly enhance mechanical, thermal, and electronic properties, even with minimal CNT incorporation. This study delves into the synergistic effects of single-walled CNTs (SWCNTs) and maleic anhydride (MA) grafting on the mechanical behavior of polyamide 6 nanocomposites, leveraging molecular dynamics simulations to dissect the influence of SWCNT chirality and MA concentration variations. Focusing on SWCNTs of (8,8) chirality, in this study, the composite's Young's modulus, tensile strength, free volume, and atomic local shear strain were evaluated across a spectrum of MA weight percentages (4.1, 8, and 12%). Our findings illuminate the critical role of SWCNT chirality in enhancing composite properties, with a notable increase in mechanical strength observed at optimal MA concentrations. Additionally, the study sheds light on the local structural transformations within the composite, particularly in relation to free volume and atomic local shear strain, under varying tensile strains. The interplay between SWCNT reinforcement and MA grafting emerges as a pivotal factor in tailoring the composite's mechanical properties, underscoring the potential of this dual-modification strategy for developing high-performance nanocomposites.

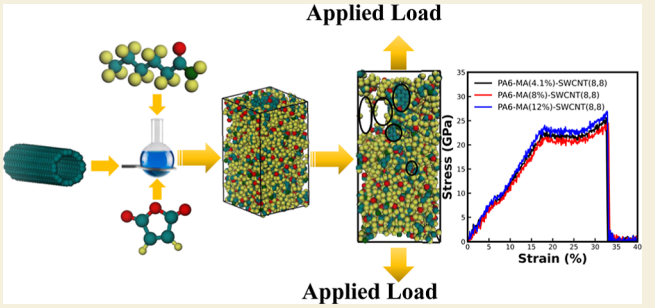

KEYWORDS: *CNT, molecular dynamics, polymer, composites, chirality*

INTRODUCTION

The integration of carbon nanotubes (CNTs) into polymer matrices to form nanocomposites significantly augments their mechanical properties, rendering these materials highly suitable for applications across a broad spectrum of industries, notably in the automotive and aerospace sectors.[1−3] The incorporation of CNTs and other nanofillers into polymers not only enhances thermal characteristics[4] but also improves structural and mechanical properties,[5] electrical conductivity,[6] optical absorption,[7] and energy storage capabilities.[8]

Polyamide 6 (PA6) stands out among thermoplastic polymers due to its superior blend of properties, making it extensively utilized across diverse sectors. PA6 exhibits remarkable mechanical performance, including a high tensile strength of 64.7 MPa, allowing it to elongate up to 51.53% of its original length before failure. Its impact strength is measured at 10.98 KJ/m^2,[9] while its thermal conductivity is reported to be 0.27 W m^{-1} K^{-1}.[10] Differential scanning calorimetry (DSC) reveals that PA6 has a glass transition temperature of 58.7 °C, and its specific heat capacity at 25 °C is 1.43824 J g^{-1} K^{-1}.[11] Further enhancing its utility, PA6 has been effectively combined with carbon fibers[12] and montmorillonite clay,[13] achieving targeted improvements in performance. Such composites find extensive use in the electrical[14] and biomedical industries,[15] underlining the versatility of PA6-based materials. The investigative focus on PA6 composites has employed a plethora of experimental methodologies to elucidate their characteristics. For instance, research by Bhattacharyya has demonstrated a progressive decline in the tensile strength and modulus of PA6 composites with increasing weight percentages of ethylene vinyl acetate (EVA).[16] In another study, Gaojie Si illustrated that expandable graphite (EG) could serve as a fire retardant, enhancing flame retardance while simultaneously impacting the mechanical properties and wear performance of a specific PA6 composite formulation (85% PA6, 15% glass fiber (GF), 5% each of polytetrafluoroethylene (PTFE), ultrahigh-molecular-weight polyethylene (UHMWPE), and colloid graphite (CG) by weight) negatively.[17]

Beyond the conventional fillers previously discussed, recent research has identified nanostructured materials, including

Received: March 7, 2024
Revised: May 16, 2024
Accepted: May 16, 2024
Published: May 28, 2024

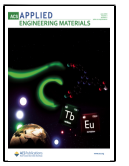

https://doi.org/10.1021/acsaenm.4c00155
ACS Appl. Eng. Mater. 2024, 2, 1593−1602

nanowires,[18] nanoplatelets,[19] nanoparticles,[20] nanotubes,[21] and nanorods,[22] as possessing a significantly greater potential to enhance specific properties of polymers compared to their bulk counterparts. For instance, Qi-Jie Xu's investigations reveal that with an incremental addition of copper nanowires, the tensile strength of nano-Cu/PA6 nanocomposites escalates, reaching a zenith at a 0.5% concentration of copper nanowires, at which point the strength peaks at 55.2 MPa, marking a 77.4% increase over pure PA6.[23] Similarly, Baoli's research demonstrates that the inclusion of 3 phr of functionalized titanium dioxide (TiO_2) nanoparticles into nanocomposites augments tensile and impact strength by 14 and 20%, respectively.[24] Further, Qijie's study on the infusion of CuO nanoparticles into the PA6 matrix at concentrations of 0.1 and 0.3% noted a marked enhancement in tensile strength, with the 0.3% CuO composite achieving a maximum strength of 45.7 MPa, a 47.5% improvement over pure PA6.[25]

In the realm of enhancing the mechanical properties of nanofillers, Ajori conducted multiple molecular dynamics (MD) simulations[26,27] to explore strategies for optimizing the mechanical characteristics of various nanofillers. These modified nanofillers were then leveraged to fortify the mechanical properties of composite materials. For example, Parsapour's work[28] investigates the tensile behavior of Cu−Zr metallic glass nanocomposites reinforced with nanowires, CNTs, and NW-encapsulated CNTs through MD simulations. The findings highlight that composites, particularly those reinforced with individual CNTs, display superior ultimate strength. Extensive research underscores the exceptional electrical,[29] electrochemical,[30] biological,[31] mechanical,[32] and optical[33] properties of CNTs, positioning them above many other metallic nanostructures in performance. Their potent antimicrobial capabilities[34] have spurred both research and practical applications.[35] Therefore, integrating CNTs into the PA6 matrix is anticipated to significantly enhance its mechanical properties.[36] Illustratively, WD Zhang's study evidence that introducing merely 1 wt % of MWNTs to PA6 substantially boosts its elastic modulus by 115%, from 396.0 to 852.4 MPa, and increases the tensile strength at yield by 124%, from 18.0 to 40.3 MPa.[37] Similarly, Yongjin's exploration into incorporating approximately 1.8 wt % of CNTs into the PVDF/PA6 blend not only elevated its conductivity from 1×10^{-13} to 0.4 S/cm but also significantly improved its mechanical properties, especially ductility.[38]

Drawing from the wealth of experimental evidence, it becomes apparent that the integration of CNTs as a reinforcing agent significantly bolsters the mechanical attributes of PA6. Despite these advancements, attaining a nuanced comprehension of the interactions between PA6 and CNTs, which underpin the observed enhancements in mechanical properties, presents a considerable challenge when relying solely on experimental methodologies. Thus, several computer simulation techniques can serve as useful substitutes to effectively illustrate the atomic-scale process of interaction between PA6 and CNTs. MD simulations are a formidable investigative technique that may be used to analyze atom-to-atom interactions based on precise interaction potentials. Ling's application of MD simulations to probe the tribological behavior arising from the sliding contacts between polymers[39] is a testament to the method's efficacy. Similarly, Frankland's exploration into the structural configurations of nanotubes—distinguishing between extended continuous and abbreviated discontinuous fibers—uncovered significant increases in composite stiffness with longer nanotubes, surpassing that of the polymer alone.[40] Hossein's MD simulations delved into the interactions at the interface between oligomeric polyamide-6,6 chains, consisting of 10 chemical repeat units, and CNTs. The study highlighted an increase in organized layered structures and a higher density of robust hydrogen bonds (HBs) at specific distances, indicating a more substantial interaction compared to bulk samples.[41]

Further illustrating the utility of MD simulations in enhancing our understanding of PA6's mechanical property augmentation, William's research demonstrated the potential of graphene (G) and CNTs to ameliorate PA6 materials, provided that voids within the nanocomposite are uniformly distributed.[42] CR Chiang and FC Chang's experimentally work on the miscibility of styrene-maleic anhydride copolymer (8% MA) with poly(2,6-dimethyl-1,4-phenylene oxide) forming graft copolymers with PA6, underscored the significant reduction in interfacial tension and the creation of finer dispersed domains, thereby enhancing mechanical properties.[43] Hassan and Othman's study revealed that integrating 10 wt % maleic anhydride polyethylene octene elastomer (POEgMAH) into PA6/polypropylene (PA6/PP) blends markedly improved toughness.[44]

While the enhancement of mechanical and electrical properties through CNT−PA6 composites and MA−PA6 graft polymers is well-documented, the exploration of maleic anhydride's (MA) role in mitigating void formation within PA6−SWCNT composites remains uncharted territory. This investigation leverages MD simulations to elucidate the influence of MA on the prevalence of voids within PA6−SWCNT systems, offering new insights into the optimization of nanocomposite materials for advanced engineering applications. The most stable molecular arrangements within nanocomposites, focusing on minimizing their overall energy and enhancing their mechanical properties are estimated. The results hold great promise for future advancements in the field of polymer−nanoparticle systems. The mechanical properties of polyoxymethylene (POM)/CNT composites have been successfully investigated in a prior work using the same simulation process.[45] We posit that the molecular modeling technique employed in this study offers a comprehensive exploration of atomic-scale local structural deformation and free space volume within the PA6/SWCNT and PA6/MA/SWCNT composites under tensile stress conditions.

COMPUTATIONAL METHODS

Interatomic Interactions

Large-scale Atomic/Molecular Massively Parallel Simulator (LAMMPS), a MD simulations software,[46] was used to probe the mechanical properties of PA6−CNT nanocomposites. Throughout these analytical processes, the ReaxFF reactive force field[47] was harnessed to delineate both the bonded and nonbonded interactions manifest within the PA6−CNT nanocomposite architectures. Renowned for its proficiency in simulating the dynamic behavior of a wide array of materials spanning both organic and inorganic domains,[47,48] the ReaxFF framework is particularly adept at capturing the complex interplay of forces at the molecular level. The computational model hinges on the ReaxFF force field's ability to calculate the system's total energy by summing various contributory energy components, as delineated in the seminal publications.[47] Specifically, the total energy (E_{system}) of the nanocomposite system is determined by the following equation

https://doi.org/10.1021/acsaenm.4c00155
ACS Appl. Eng. Mater. 2024, 2, 1593−1602

$$E_{system} = E_{bond} + E_{over} + E_{under} + E_{val} + E_{pen} + E_{tors} + E_{conj} + E_{vdWals} + E_{coulomb} \quad (1)$$

where E_{bond}, E_{over}, E_{under}, E_{val}, E_{pen}, E_{tors}, E_{conj}, E_{vdWals}, and $E_{coulomb}$ represent the energies associated with bond stretching, penalties for atom overcoordination, penalties for atom under-coordination, valence angle deformations, penalties for angle overcoordination and under-coordination, torsional angle variations, effects of conjugation on molecular energy, nonbonded van der Waals interactions, and Coulombic interactions within the nanosystem, respectively.

To validate the application of ReaxFF in our research, we examined a (8,8) armchair CNT with dimensions of 49.19 Å in length and 10.85 Å in diameter. ReaxFF was employed to model carbon interactions, and the system underwent minimization and deformation to assess stress and strain, ultimately determining Young's modulus.

The outcomes for the CNT align well with experimental findings, with minor disparities attributed to variations in CNT diameter and the presence of defects reported by Kamal et al.[49] It is noted that defects in CNT, as highlighted in the experimental samples, can significantly impact modulus values. Other studies by Krishnan et al.[50] utilizing thermal vibration, Salvetat et al.[51] employing an atomic force microscope on clamped nanotubes, and simulations by WenXing et al.[52] and Qiang et al.[53] through MD also contribute comparable results to our simulations, affirming the effectiveness and accuracy of ReaxFF (refer to Table 1).

Table 1. Analyzing Young's Modulus of Carbon Nanotubes in Comparison with Existing Literature Values

investigations	Young's modulus (GPa)
present work	1277.277521
Krishnan et al. [experimental][50]	900−1700
Salvetat et al. [experimental][51]	800 ± 410
WenXing et al. [REBO and LJ potential][52]	935.805 ± 0.618
Qiang et al. [Morse potential][53]	840 ± 20

This comprehensive approach enables the nuanced simulation of PA6−CNT nanocomposites, capturing the essence of their mechanical behavior under various conditions. The utilization of the ReaxFF force field, with its detailed accounting for a spectrum of energy contributions, underscores the sophistication and precision of current computational methodologies in elucidating the molecular foundations of material properties.

Molecular Model

In-depth compositions and structures that are essential to comprehending the characteristics and behaviors of different materials are covered in the Molecular Model section. In this section, we examine four different molecular models, each providing a special perspective on a certain facet of molecular interactions. These subsections offer a thorough examination of molecular arrangements and their consequences in material science, ranging from the basic PA6 Matrix model to the sophisticated MA-grafted nanocomposite model.

PA6 Matrix Model. In the construction of the PA6 matrix model, a polymer chain comprising 20 repetitive nylon-6 units was synthesized. This polymer chain was subsequently subjected to a packing process within the simulation box, facilitated through geometry optimization techniques. The packing protocol entailed the random distribution of nylon-6 polymer chains within the confines of a simulation box, imposing periodic boundary conditions to emulate the initial nanocomposite structure. This methodology yielded a material density of 1.084 g/cm^3. The primary unit cell adopted a tetragonal shape, characterized by dimensions of 30, 30, and 49.19 Å along the x, y, and z axes, respectively, under periodic boundary conditions as depicted in Figure 1. It is imperative to acknowledge that, due to computational constraints inherent in MD simulations, the polymer models utilized are considerably shorter than their real-world analogues. An alternative strategy involves employing polymer models capable of mirroring the material properties exhibited by longer polymer chains, thus overcoming computational limitations.

SWCNT Model. CNTs are classified into single-walled,[54] double-walled,[55] or multiwalled[56] variants, contingent upon the number of concentric cylindrical layers constituting their structure. Within the domain of polymer nanocomposites, theoretical models predominantly leverage either infinite or capped single-walled CNTs (SWCNTs) to simulate the reinforcement effect attributed to these nanomaterials.[57] The properties of SWCNTs are notably influenced by their structural nuances, including chirality and wall configuration.[58,59] Our study focuses on armchair SWCNTs, selected for their superior reinforcement potential[60] and exceptional elongation attributes.[61] Specifically, armchair SWCNTs with chiralities of (4,4) and (8,8), corresponding to diameters of 5.42 and 10.85 Å, respectively, were chosen for detailed examination. Both SWCNT models were standardized to a length of 49.19 Å, with the study

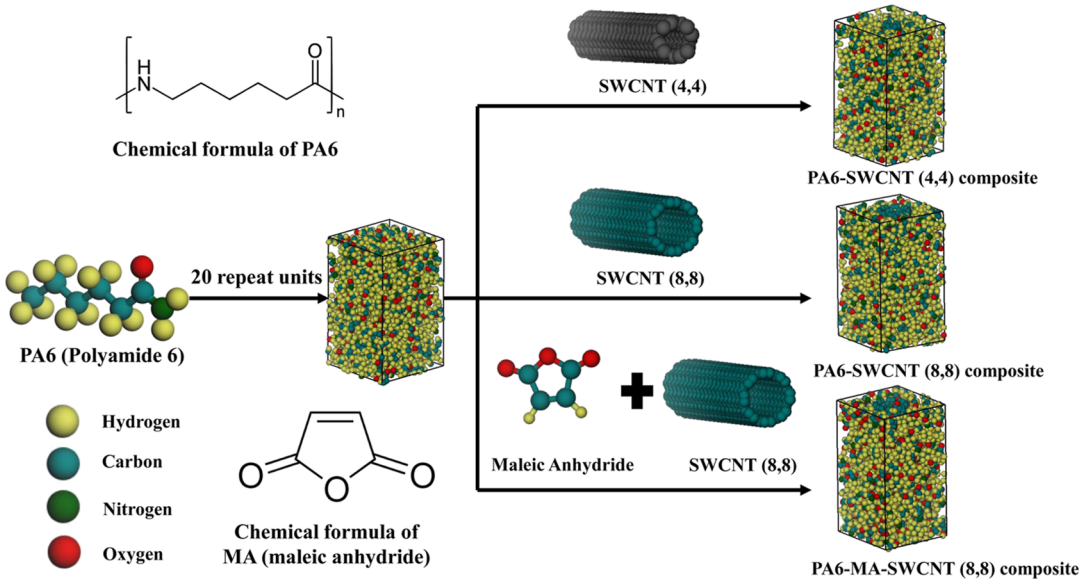

Figure 1. Representation of the preparation process of PA6−MA−SWCNT and PA6−SWCNT.

https://doi.org/10.1021/acsaenm.4c00155
ACS Appl. Eng. Mater. 2024, 2, 1593−1602

Table 2. Simulation Details for Various PA6−SWCNT Composites with Varying MA Content and Chirality

	box dimensions Å^3	number of PE chains	total atom numbers
PA6−SWCNT (4,4)	30 × 30 × 49.19	11	4522
PA6−SWCNT (8,8)	30 × 30 × 49.19	9	4078
PA6−MA (4.1%)−SWCNT (8,8)	30 × 30 × 49.19	9	4159
PA6−MA (8%)−SWCNT (8,8)	30 × 30 × 49.19	9	4231
PA6−MA (12%)−SWCNT (8,8)	30 × 30 × 49.19	8	3930

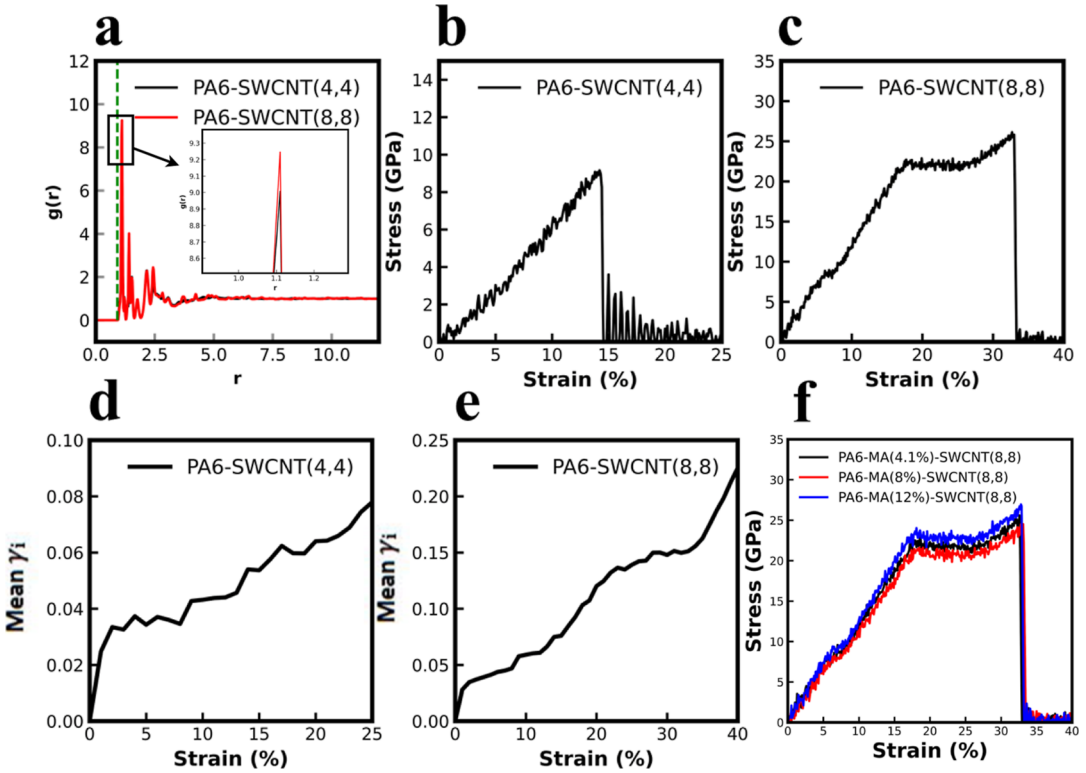

Figure 2. (a) RDF profiles for the PA6 matrix surrounding the carbon atoms of the CNT, (b) stress−strain curves of PA6−SWCNT (4,4), (c) stress−strain curves of PA6−SWCNT (8,8), (d) strain-dependent mean Von Mises shear strain profiles for PA6−SWCNT (4,4), (e) strain-dependent mean Von Mises shear strain profiles for PA6−SWCNT (8,8), and (f) stress−strain curves for PA6−MA (4.1%)−SWCNT (8,8), PA6−MA (8%)−SWCNT (8,8), and PA6−MA (12%)−SWCNT (8,8).

design not accounting for the impact of SWCNT length on the behavior of the model.

PA6 SWCNT Nanocomposite Model. The investigation into the effects of SWCNT diameter variations within PA6−SWCNT nanocomposites culminated in the development of two distinct models: PA6−SWCNT (4,4) and PA6−SWCNT (8,8). Each configuration was encapsulated within a tetragonal unit cell, with x and y dimensions measuring 30 Å and a z dimension of 49.19 Å, as illustrated in Figure 1. Table 2 presents a comparative analysis of system sizes at zero strain for all simulation models, facilitating a systematic comparison by detailing the number of PA6 chains and the total atom count under uniform strain conditions.

MA-Grafted Nanocomposite Model. The exploration of maleic anhydride (MA)'s effect on the PA6/SWCNT composites led to the creation of three variant composites, each incorporating different weight fractions of MA (4.1, 8, and 12%) within a base PA6−SWCNT (8,8) framework. Analogous to the pristine PA6−SWCNT composites, all MA-grafted models featured a tetragonal unit cell structure, with x and y dimensions maintained at 30 Å and a z-dimension of 49.19 Å (Figure 1).

MD Simulations. Initially, a single PA6 polymer chain, MA structure, and CNT crystal were constructed. Subsequently, the polymer chain was arranged around the SWCNT for PA6−SWCNT composites. Similarly, for PA6−MA−SWCNT, both the polymer chain and MA structure were positioned around the SWCNT. To ensure seamless integration with the Large-Scale Atomic/Molecular Massively Parallel Simulator (LAMMPS), Visual Molecular Dynamics (VMD)[62] was utilized for both the conversion of the model and the subsequent post-processing activities. Thereafter, the ultimate MD simulation is conducted using the LAMMPS software. The formation of interfacial covalent bonds between CNTs and PA6 in nanocomposites is fundamentally contingent upon the intermolecular distance at their juncture. In our investigation, we facilitated robust CNT−PA6 interfacial bonding by minimizing this intermolecular distance, thereby obviating steric hindrances and enabling effective interactions between the carbon atoms of the CNT and the functional groups of the PA6 chains. A constant time step of 0.1 fs was adopted for the integration of simulation trajectories throughout the study.

To adequately prepare the nanocomposite system for uniaxial tensile testing, the system first experienced energy minimization using the conjugate gradient algorithm. The minimization process was defined with a stopping tolerance for energy set at 1×10^{-32}, for force set at 1×10^{-6}, and a limit on iterations set to 5000. Following this, the system was simulated in the microcanonical ensemble (NVE), maintaining a constant number of atoms, volume, and energy, for 1 ps, during which it was heated to the target temperature of 300 K. Then, the system undergoes a relaxation phase within the isothermal−isobaric ensemble (*NPT*) for a minimum duration of 5 ps. The target temperature and pressure during this NPT relaxation are maintained at 300 K and 1 atm, respectively. Subsequently, the system transitions

https://doi.org/10.1021/acsaenm.4c00155
ACS Appl. Eng. Mater. 2024, 2, 1593−1602

to a canonical ensemble (*NVT*) for equilibration, lasting another 5 ps. Throughout this *NVT* equilibration, the system's temperature was independently controlled using Nose−Hoover thermostat[63] to ensure a constant temperature of 300 K. Uniaxial deformation along the *z*-axis at 300 K was performed within the canonical ensemble (*NVT*) setup to ensure precise control over temperature fluctuations during the testing. A strain rate of 10^{11} s^{-1} was applied throughout the deformation process to simulate realistic deformation speeds that approximate experimental strain rates,[64] facilitating the generation of a detailed stress−strain curve. Analysis of this curve enabled the accurate assessment of essential mechanical properties, including the ultimate stress, breaking strain, and Young's modulus, thereby providing profound insights into the material's behavior under stress.

RESULTS AND DISCUSSION

Structural Analysis

The radial distribution function (RDF) serves as a pivotal tool in statistical mechanics for elucidating the degree of attraction between particles or molecules. Specifically, the RDF quantifies the likelihood of locating a particle (B) at a defined distance from a reference particle (A), thereby offering insights into the variation in density of atoms or particles as a function of distance. Mathematically, the RDF is articulated as[65]

$$g_{A-B} = \frac{n_B/(4\pi r^2 \Delta r)}{N_B/V} \quad (2)$$

where n_B denotes the count of atoms B within a spherical shell encircling atom A, spanning the distance range $r \sim (r + \Delta r)$. Here, V represents the volume of the simulation box, and N_B is the aggregate number of atoms B.

Figure 2a delineates the RDF profiles for PA6 in interaction with CNTs for two distinct materials: PA6−SWCNT (4,4) and PA6−SWCNT (8,8). A critical observation is that the RDF's origin in PA6−SWCNT composites is anchored at the CNT surface, with the dashed line demarcating the interfacial region. The RDF graphs for both materials exhibit significant overlap, suggesting a similar spatial arrangement of molecules around the CNTs. A pronounced peak is observed at 1.1 Å, proximal to the CNT surface. This peak, being sharper than subsequent peaks, signifies the strongest interaction between PA6 and the CNT within a 1.1 Å vicinity, indicative of a locally high density and robust interaction strength correlating to the CNT. Upon examination, it is discernible that the $g(r)$ value for PA6−SWCNT (8,8) surpasses that of PA6−SWCNT (4,4) at the first peak, implying a more substantial interaction energy between the PA6 chains and CNT in the case of SWCNT (8,8) compared to that of SWCNT (4,4). This phenomenon can be attributed to the increased surface contact area facilitated by a larger radius of CNTs, thereby enhancing the interaction energy.

Stress−Strain Analysis

The stress versus strain behavior of each system is elucidated through the graphical representations provided in Figure 2b,c. Consistent with prior research, the spatial orientation of polymer chains within nanocomposites exhibits a preferred alignment around SWCNTs, which significantly augments the mechanical properties of the nanocomposites, as evidenced by an increase in both bulk and Young's moduli.[66] A paramount factor in achieving enhanced composite materials is the efficient stress transfer from the matrix to the nanofillers.

Figure 2b illustrates the brittle fracture behavior observed in the PA6−SWCNT (4,4) nanocomposite. This composite exhibits a linear elastic response from 0 to 14% strain, indicating a proportional increase in stress with strain up to its ultimate stress. Beyond this point, a significant decrease in stress is observed, culminating nearly at 0 GPa, as the SWCNT breaks. Conversely, the PA6−SWCNT (8,8) composite, as depicted in Figure 2c, demonstrates an elastic behavior from 0 to 17.7% strain, with a linear stress increase up to 22.7 GPa. Subsequently, a plateau is observed until 28% strain, followed by a parabolic increase in stress, reaching a peak before precipitously decreasing to 0 GPa.

Table 3 presents the key mechanical properties derived from these stress−strain curves. The Young's modulus for each composite is determined through nonlinear regression analysis,[67] with the PA6−SWCNT (4,4) and PA6−SWCNT (8,8) composites yielding Young's moduli of 66.07 and 122.32 GPa, respectively. Thus, the inclusion of an SWCNT with armchair configuration (8,8) results in an 85.14% increase in Young's modulus compared to the SWCNT (4,4). Ultimate stress values for the PA6−SWCNT (4,4) and PA6−SWCNT (8,8) are 9.16 and 26.12 GPa, respectively, indicating a substantial increase of approximately 185.15%.

Table 3. Young's Modulus and Ultimate Stress for PA6−SWCNT (4,4) and PA6−SWCNT (8,8)

single wall carbon nano tube	(4,4)	(8,8)
Young's modulus (GPa)	66.07	122.32
tensile strength (GPa)	9.16	26.12

Employing CNTs with a larger diameter has been shown to elevate both the Young's modulus and ultimate stress of composite materials.[45] In this study, the diameter of SWCNTs with chirality (8,8) is roughly twice that of SWCNTs with chirality (4,4), leading to ascend both the Young's modulus and ultimate stress in the PA6−SWCNT (8,8) composite compared to that in the PA6−SWCNT (4,4) composite. This disparity in mechanical behavior is distinctly manifested in the stress−strain profiles of each composite.

Local Structural Rearrangements

The atomic local shear strain serves as a quantitative measure for deformation within a system under shear stress, providing insights into the mechanical behavior of a system's particles under a spectrum of loading conditions. Such a metric is instrumental for examining the genesis of cracks and other material defects. Even under minimal stress, the atomic local shear strain can pinpoint localized zones where irreversible material distortion commences, information that is crucial for predicting yield strength and plasticity of materials. The atomic local shear strain or Von Mises shear strain (γ_i) emerges as a robust measure for local shear deformation, independent of deformation direction, and can be quantified using eq 3[68]

$$\gamma_i = \left[E_{xy}^2 + E_{xz}^2 + E_{yz}^2 + \frac{1}{6}((E_{xx} - E_{yy})^2 + (E_{yy} - E_{zz})^2 + (E_{zz} - E_{xx})^2)\right]^{0.5} \quad (3)$$

An elevated γ_i value signifies that an atom is undergoing considerable shear and plastic deformation locally, whereas a lower value indicates minor relative movement of the atom with respect to its nearest neighbors.[69]

Mean γ_i values for PA6−SWCNT (4,4) across all strain rates are graphically represented in Figure 2d. At the undeformed

https://doi.org/10.1021/acsaenm.4c00155
ACS Appl. Eng. Mater. 2024, 2, 1593−1602

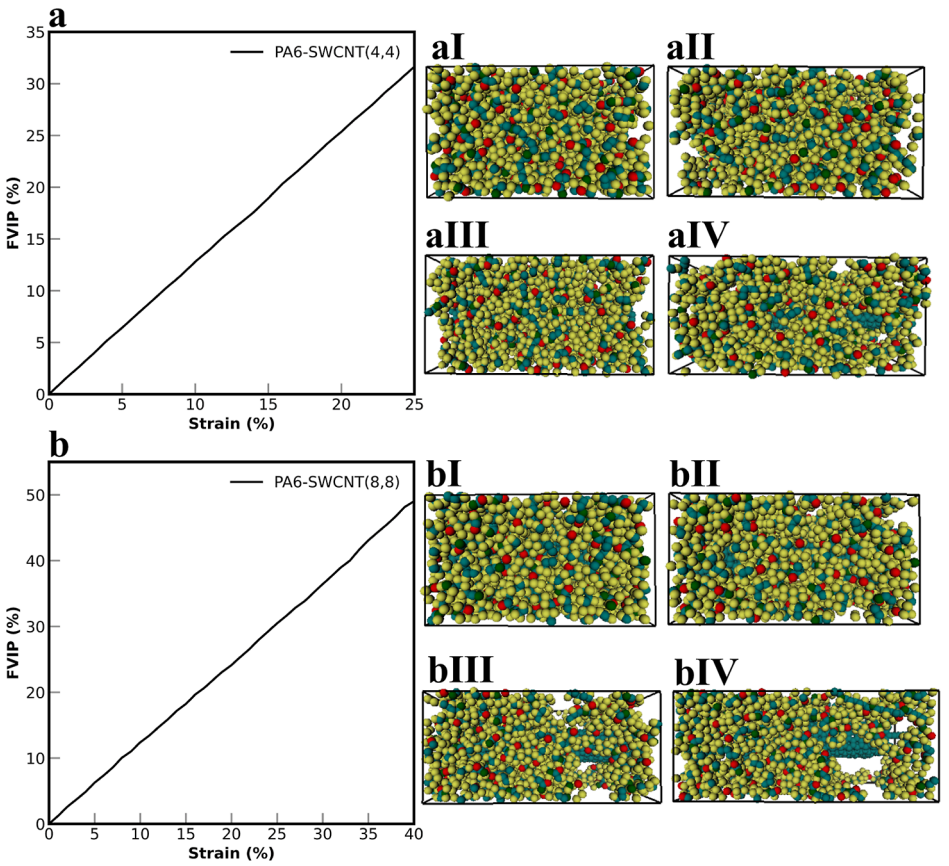

Figure 3. (a) Diagram depicting the rise in percentage of free volume for PA6−SWCNT (4,4), uniaxial tensile deformation in PA6−SWCNT (4,4) for strain = (aI) 0%, (aII) 14% (ultimate stress), (aIII) 20%, and (aIV) 25%, (b) diagram depicting the rise in percentage of free volume for PA6−SWCNT (8,8), and uniaxial tensile deformation in PA6−SWCNT (8,8) for strain = (bI) 0%, (bII) 12%, (bIII) 24%, and (bIV) 40%.

state (0% strain), γ_i values for the majority of atoms are near zero, with a mean of 1.06×10^{-16}, denoting an absence of significant deformation or slippage between adjacent atomic planes (Figure 3aI). Notably, regions within PA6−SWCNT (4,4) exhibit atoms with elevated γ_i values at the strain corresponding to ultimate stress. The analysis of mean gamma values, as depicted in Figure 2d, underscores that local elastic deformation predominates within the material from 0 to 14% strain, with an absence of discernible voids (Figure 3aII). Beyond the ultimate stress, the PA6−SWCNT (4,4) system begins to form voids, particularly in localized zones marked by higher γ_i values, suggesting the onset of significant material failure (Figure 3aIII). These voids propagate as the strain exceeds the ultimate stress threshold, accompanied by an increase in γ_i values for atoms in the vicinity, indicative of severe and localized shear deformation. Moreover, with increasing strain, these voids exhibit progressive enlargement, becoming markedly more pronounced at 25% strain compared to the unstrained state (Figure 3aIV).

Figure 2e delineates the correlation between strain and the Von Mises shear strain (γ_i) for the PA6−SWCNT (8,8) system. Within the initial strain range of 0−12%, a linear relationship is apparent; the γ_i values increase at a steady rate. Concurrent with this trend is the emergence of minuscule voids, appearing sporadically throughout the material (see Figure 3bII). As the strain intensifies, reaching 24%, a pronounced proliferation of voids is observed, as depicted in Figure 3bIII. This void formation is notably asymmetric, with a predilection for one side of the composite. Subsequent escalation of strain up to 40% witnesses the continuous growth of these voids, in tandem with a rise in the atomic γ_i values, suggesting an augmentation in localized shear deformation and material failure processes (refer to Figure 3bIV).

Local Volume Analysis

Figure 3aI−aIV,bI−bIV illustrate the emergence of excess local volume, conventionally termed as free volume, throughout the tensile deformation process. The extent of free volume at a particular strain magnitude is determined through the equation

$$\mathrm{FV}(\varepsilon) = \mathrm{CV}(\varepsilon) - \sum_{i=1}^{N} \mathrm{PV}(\varepsilon) \tag{4}$$

where FV represents the free volume, CV the cell volume, and PV the particle volume at a given strain ε was computed using Connolly surface method,[70] where Connolly radius was 1.0 Å and solvent radius was 0.0 Å. The increase in free volume in percentage (FVIP) is defined and computed as follows

$$\mathrm{FVIP}(\varepsilon) = \frac{\mathrm{FV}(\varepsilon) - \mathrm{FV}(0)}{\mathrm{FV}(0)} \times 100\% \tag{5}$$

The progression of FVIP for PA6−SWCNT (4,4) and PA6−SWCNT (8,8) across varying levels of strain is presented in Figure 3a,b, respectively. For both nanocomposite systems, there is an observed incremental rise in FVIP with enhanced strain. This increment indicates that with the increase in strain, the void sizes within the matrix correspondingly expand. Notably, the steeper slopes of 1.26 and 1.22 in Figure 3a,b,

https://doi.org/10.1021/acsaenm.4c00155
ACS Appl. Eng. Mater. 2024, 2, 1593−1602

respectively, allude to a relatively lower FVIP for the PA6−SWCNT (8,8) composite. This observation implies that the interaction between CNT (8,8) and the PA6 chains significantly fortifies the mechanical integrity of the PA6 matrix when compared to the interactions facilitated by CNT (4,4).

Stress−Strain Analysis for MA-Grafted Composites

Figure 2f delineates the mechanical properties of PA6 grafted with maleic anhydride (MA) and reinforced with SWCNTs possessing (8,8) chirality. Table 4 aggregates the principal mechanical findings of this study. The integration of maleic anhydride into the PA6−SWCNT (8,8) composite was performed at varying weight percentages (4.1, 8, and 12%). Subsequent to this modification, the Young's modulus of the composites was ascertained to be 120.767, 115.648, and 126.628, GPa, respectively. It was observed that the incorporation of 4.1 and 8% MA into PA6−SWCNT (8,8) composites resulted in a decrement in the Young's modulus by approximately 1.27 and 5.45%, respectively, relative to the ungrafted composite. In contrast, the introduction of 12% MA led to an enhancement in Young's modulus by approximately 3.52%.

Table 4. Young's Modulus and Ultimate Stress for PA6−SWCNT (8,8) at Different MA Weight Fractions

MA weight fraction (%)	4.1	8	12
Young's modulus (GPa)	120.767	115.648	126.628
tensile strength (GPa)	25.584	24.514	26.95

The influence of MA content on the ultimate stress of PA6-SWCNT (8,8) composites is also listed in Table 4. Relative to the pristine composite (26.12 GPa), the inclusion of 4.1% MA resulted in an ultimate stress of 25.584 GPa, which marks a reduction of about 2.05%. This reduction is further exacerbated with 8% MA, where the ultimate stress diminishes to 24.514 GPa, amounting to a decrease of 6.15%. Contrariwise, at a 12% MA concentration, there is an observable augmentation in ultimate stress to 26.95 GPa, which constitutes an increase of 3.18% over the unmodified composite.

Maleic Anhydride-Induced Free Volume Reduction

As depicted in Figure 4a, the integration of 8% maleic anhydride (MA) into the PA6−SWCNT (8,8) composite appears to reduce the free volume. At a strain level of 40%, the free volume increase percentage (FVIP) for the MA-8% composite registers at 48.77%, in contrast to the 49.02% observed for the ungrafted PA6−SWCNT (8,8) composite. Conversely, a lower MA concentration of 4.1% demonstrates disparate free volume dynamics. At a strain of 18%, the FVIP for the 4.1% MA composite is the smallest (20.77%) among the composites under investigation. Remarkably, by the point of 40% strain, the 4.1% MA composite exhibits the most substantial FVIP value. In the meantime, the composite containing 12% MA displays a FVIP commensurate with that of the unmodified PA6−SWCNT (8,8) across the entire spectrum of applied strain.

Notably, while the PA6−MA (8%)−SWCNT (8,8) composite shows the most diminished FVIP, as evidenced in Figure 4a, it concurrently manifests the most inferior mechanical characteristics among the composites evaluated within this study, as delineated in Figure 2f.

CONCLUSIONS

This study has systematically explored the mechanical properties and structural dynamics of PA6 nanocomposites reinforced with SWCNTs, both unmodified and grafted with varying weight percentages of maleic anhydride (MA). Conducting meticulous MD simulations, the stress−strain behavior, evolution of atomic shear strain, and variation in free volume under tensile loading have been analyzed. Our findings reveal that the incorporation of SWCNTs significantly enhances the Young's modulus and tensile strength of the PA6 matrix, with the chirality and diameter of the SWCNTs being key factors influencing the mechanical properties.

The introduction of MA to the PA6−SWCNT composites was observed to have a dichotomous effect on the mechanical properties. While lower percentages of MA grafting (4.1 and 8%) resulted in a reduction of the Young's modulus, a higher

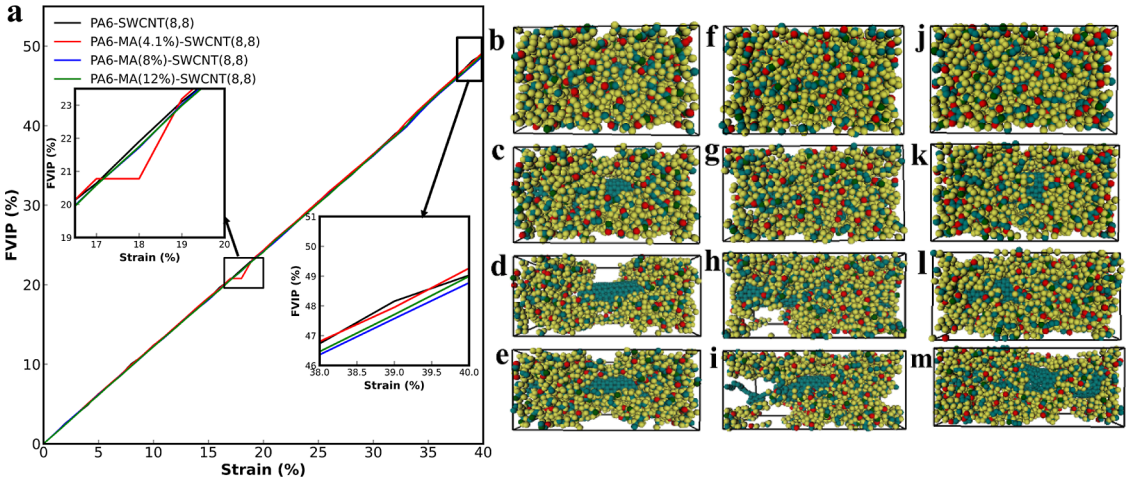

Figure 4. (a) Diagrams of increase in percentage of free volume for PA6−MA (4.1%)−SWCNT (8,8), PA6−MA (8%)−SWCNT (8,8), and PA6−MA (12%)−SWCNT (8,8), uniaxial tensile deformation in PA6−MA (4.1%)−SWCNT (8,8) for strain = (b) 0%, (c) 12%, (d) 24%, and (e) 40%, in PA6−MA (8%)−SWCNT (8,8) for strain = (f) 0%, (g) 12%, (h) 24%, and (i) 40%, and in PA6−MA (12%)−SWCNT (8,8) for strain = (j) 0%, (k) 12%, (l) 24%, and (m) 40%.

https://doi.org/10.1021/acsaenm.4c00155
ACS Appl. Eng. Mater. 2024, 2, 1593−1602

percentage (12%) improved it. The stress−strain analysis elucidated the superior mechanical strength of PA6−SWCNT (8,8) composites over their (4,4) counterparts, indicating the critical role of CNT diameter in the reinforcement mechanism. Furthermore, the study provided insights into local structural rearrangements, highlighting the correlation between atomic local shear strain and the formation of voids, which in turn influenced the composite's mechanical behavior.

Despite the comprehensive nature of this research, certain limitations must be acknowledged. The MD simulations are constrained by scale and time, limiting the ability to simulate larger systems and longer timeframes that could capture the full spectrum of mechanical behaviors in real-world applications. Additionally, the models used in this study did not account for potential chemical reactions between PA6 and SWCNTs or the effects of environmental factors such as humidity and temperature.

Future work could extend this research by exploring the use of longer polymer chains in simulations to better approximate the behaviors of industrial-scale materials. Additionally, experimental validation of the simulation results would be beneficial to confirm the predicted mechanical properties in practical applications. The exploration of other types of nanofillers and functionalization methods could also provide further enhancements to the mechanical properties of polymer nanocomposites. Ultimately, the integration of computational and experimental approaches will be crucial in the ongoing development of advanced materials with tailored properties for specific engineering applications.

AUTHOR INFORMATION

Corresponding Author

A. K. M. Masud − *Department of Industrial and Production Engineering, Bangladesh University of Engineering and Technology, Dhaka 1000, Bangladesh*; Email: masud1@ipe.buet.ac.bd

Authors

Mehedi Hasan − *Department of Industrial and Production Engineering, Bangladesh University of Engineering and Technology, Dhaka 1000, Bangladesh*; orcid.org/0009-0009-9988-0434

Khayrul Islam − *Department of Mechanical Engineering and Mechanics, Lehigh University, Bethlehem, Pennsylvania 18015, United States*

Complete contact information is available at: https://pubs.acs.org/10.1021/acsaenm.4c00155

Notes

The authors declare no competing financial interest.

ACKNOWLEDGMENTS

The research funding from the Department of Industrial and Production Engineering at Bangladesh University of Engineering and Technology for conducting this research study is greatly appreciated.

REFERENCES

(1) Liu, Y.; Kumar, S. Polymer/carbon nanotube nano composite fibers−a review. *ACS Appl. Mater. Interfaces* **2014**, *6*, 6069−6087.

(2) Iqbal, A.; Saeed, A.; Ul-Hamid, A. A review featuring the fundamentals and advancements of polymer/CNT nanocomposite application in aerospace industry. *Polym. Bull.* **2021**, *78*, 539−557.

(3) Chandra, A. K.; Kumar, N. R. *Properties and applications of polymer nanocomposites: clay and carbon based polymer nanocomposites*; Springer, 2016; pp 139−172.

(4) Chen, G.; Yadav, A.; Jung, I.-W.; Lee, J.; Choi, K.; Kang, S.-W. Crosslinking effect of borax additive on the thermal properties of polymer-based 1D and 2D nanocomposites used as thermal interface materials. *Sci. Rep.* **2022**, *12*, 16029.

(5) Tjong, S. C. Structural and mechanical properties of polymer nanocomposites. *Mater. Sci. Eng., R* **2006**, *53*, 73−197.

(6) Min, C.; Shen, X.; Shi, Z.; Chen, L.; Xu, Z. The electrical properties and conducting mechanisms of carbon nanotube/polymer nanocomposites: A review. *Polym.-Plast. Technol. Eng.* **2010**, *49*, 1172−1181.

(7) Goumri, M.; Lucas, B.; Ratier, B.; Baitoul, M. Electrical and optical properties of reduced graphene oxide and multi-walled carbon nanotubes based nanocomposites: A comparative study. *Opt. Mater.* **2016**, *60*, 105−113.

(8) Bindu, M.; Periyat, P. A review on fine-tuning of energy storage characteristics of conducting polymers. *Mater. Adv.* **2023**, *4*, 2730−2769.

(9) Sathees Kumar, S.; Kanagaraj, G. Investigation on mechanical and tribological behaviors of PA6 and graphite-reinforced PA6 polymer composites. *Arabian J. Sci. Eng.* **2016**, *41*, 4347−4357.

(10) Li, M.; Wan, Y.; Gao, Z.; Xiong, G.; Wang, X.; Wan, C.; Luo, H. Preparation and properties of polyamide 6 thermal conductive composites reinforced with fibers. *Mater. Des.* **2013**, *51*, 257−261.

(11) Sohel, M. A.; Mandal, A.; Mondal, A.; Pan, S.; SenGupta, A. Thermal analysis of ABS/PA6 polymer blend using differential scanning calorimetry. *J. Therm. Anal. Calorim.* **2017**, *129*, 1689−1695.

(12) Sang, L.; Wang, C.; Wang, Y.; Wei, Z. Thermo-oxidative ageing effect on mechanical properties and morphology of short fibre reinforced polyamide composites−comparison of carbon and glass fibres. *RSC Adv.* **2017**, *7*, 43334−43344.

(13) Duleba, B.; Spišák, E.; Greškovič, F. Mechanical properties of PA6/MMT polymer nanocomposites and prediction based on content of nanofiller. *Procedia Eng.* **2014**, *96*, 75−80.

(14) Gensler, R.; Gröppel, P.; Muhrer, V.; Müller, N. Application of nanoparticles in polymers for electronics and electrical engineering. *Part. Part. Syst. Charact.* **2002**, *19*, 293−299.

(15) Zomer Volpato, F. Composites for Biomedical Applications. Ph.D. Thesis, University of Trento, 2010.

(16) Bhattacharyya, A. R.; Maiti, S.; Misra, A. Mechanical properties and morphology of PA6/EVA blends. *J. Appl. Polym. Sci.* **2002**, *85*, 1593−1606.

(17) Si, G.; Li, D.; You, Y.; Hu, X. Investigation of the influence of red phosphorus, expansible graphite and zinc borate on flame retardancy and wear performance of glass fiber reinforced PA6 composites. *Polym. Compos.* **2017**, *38*, 2090−2097.

(18) Xu, Q.; Li, X.; Zhang, S.; Hao, Y.; Zhang, Z. Copper nanowire/PA6 composites prepared by in situ polymerization and its properties. *J. Polym. Res.* **2013**, *20*, 257−266.

(19) Mayoral, B.; Harkin-Jones, E.; Khanam, P. N.; AlMaadeed, M.; Ouederni, M.; Hamilton, A.; Sun, D. Melt processing and characterisation of polyamide 6/graphene nanoplatelet composites. *RSC Adv.* **2015**, *5*, 52395−52409.

(20) Zhou, S.; Wang, F.; Balachandran, S.; Li, G.; Zhang, X.; Wang, R.; Liu, P.; Ding, Y.; Zhang, S.; Yang, M. Facile fabrication of hybrid PA6-decorated TiO 2 fabrics with excellent photocatalytic, antibacterial, UV light-shielding, and super hydrophobic properties. *RSC Adv.* **2017**, *7*, 52375−52381.

(21) Guo, B.; Zou, Q.; Lei, Y.; Jia, D. Structure and performance of polyamide 6/halloysite nanotubes nanocomposites. *Polym. J.* **2009**, *41*, 835−842.

(22) Li, L.; Yang, G. Synthesis and properties of hydroxyapatite nanorod-reinforced polyamide 6 nanocomposites. *Polym. Int.* **2009**, *58*, 380−387.

(23) Xu, Q.-J.; Li, X.-H.; Zhang, S.-M.; Zhang, Z.-J. Preparation and characterization of copper nanowire/polyamide 6 nanocomposites and its properties. *J. Macromol. Sci., Part A: Pure Appl.Chem.* **2014**, *51*, 598−603.
(24) Ou, B.; Zhou, Z.; Liu, Q.; Liao, B.; Xiao, Y.; Liu, J.; Zhang, X.; Li, D.; Xiao, Q.; Shen, S. Mechanical properties and nonisothermal crystallization kinetics of polyamide 6/functionalized TiO2 nanocomposites. *Polym. Compos.* **2014**, *35*, 294−300.
(25) Xu, Q.; Li, X.; Zhang, Z. Preparation of copper nanoparticle-improved polyamide 6 composites by an in situ solution route with cupric oxide as the metallic copper source and investigation of their properties. *New J. Chem.* **2015**, *39*, 3015−3020.
(26) Ajori, S.; Parsapour, H.; Ansari, R. Stability analysis of endohedrally functionalized carbon nanotubes with pentagonal metallic nanowires: a molecular dynamics simulation approach. *Mater. Res. Express* **2019**, *6*, 045056.
(27) Ajori, S.; Parsapour, H.; Ansari, R. Structural properties and buckling behavior of non-covalently functionalized single-and double-walled carbon nanotubes with pyrene-linked polyamide in aqueous environment using molecular dynamics simulations. *J. Phys. Chem. Solids* **2019**, *131*, 79−85.
(28) Ajori, S.; Parsapour, H.; Ansari, R. A comprehensive analysis of the mechanical properties and fracture analysis of metallic glass nanocomposites reinforced by carbon nanotubes and Cu nanowires: a molecular dynamics study. *Mech. Adv. Mater. Struct.* **2021**, *28*, 2531−2550.
(29) Wang, J.; Luo, X.; Wu, T.; Chen, Y. High-strength carbon nanotube fibre-like ribbon with high ductility and high electrical conductivity. *Nat. Commun.* **2014**, *5*, 3848.
(30) Gabay, T.; Ben-David, M.; Kalifa, I.; Sorkin, R.; Abrams, Z. R.; Ben-Jacob, E.; Hanein, Y. Electro-chemical and biological properties of carbon nanotube based multi-electrode arrays. *Nanotechnology* **2007**, *18*, 035201.
(31) Wei, W.; Sethuraman, A.; Jin, C.; Monteiro-Riviere, N.; Narayan, R. Biological properties of carbon nanotubes. *J. Nanosci. Nanotechnol.* **2007**, *7*, 1284−1297.
(32) Arash, B.; Wang, Q.; Varadan, V. Mechanical properties of carbon nanotube/polymer composites. *Sci. Rep.* **2014**, *4*, 6479.
(33) Allsop, T.; Arif, R.; Neal, R.; Kalli, K.; Kundrát, V.; Rozhin, A.; Culverhouse, P.; Webb, D. J. Photonic gas sensors exploiting directly the optical properties of hybrid carbon nanotube localized surface plasmon structures. *Light: Sci. Appl.* **2016**, *5*, No. e16036.
(34) Yang, C.; Mamouni, J.; Tang, Y.; Yang, L. Antimicrobial activity of single-walled carbon nanotubes: length effect. *Langmuir* **2010**, *26*, 16013−16019.
(35) Anzar, N.; Hasan, R.; Tyagi, M.; Yadav, N.; Narang, J. Carbon nanotube-A review on Synthesis, Properties and plethora of applications in the field of biomedical science. *Sens. Int.* **2020**, *1*, 100003.
(36) Gao, J.; Itkis, M. E.; Yu, A.; Bekyarova, E.; Zhao, B.; Haddon, R. C. Continuous spinning of a single-walled carbon nanotube- nylon composite fiber. *J. Am. Chem. Soc.* **2005**, *127*, 3847−3854.
(37) Zhang, W. D.; Shen, L.; Phang, I. Y.; Liu, T. Carbon nanotubes reinforced nylon-6 composite prepared by simple melt-compounding. *Macromolecules* **2004**, *37*, 256−259.
(38) Li, Y.; Shimizu, H. Conductive PVDF/PA6/CNTs nanocomposites fabricated by dual formation of cocontinuous and nanodispersion structures. *Macromolecules* **2008**, *41*, 5339−5344.
(39) Dai, L.; Minn, M.; Satyanarayana, N.; Sinha, S. K.; Tan, V. Identifying the mechanisms of polymer friction through molecular dynamics simulation. *Langmuir* **2011**, *27*, 14861−14867.
(40) Frankland, S.; Harik, V.; Odegard, G.; Brenner, D.; Gates, T. The stress−strain behavior of polymer−nanotube composites from molecular dynamics simulation. *Compos. Sci. Technol.* **2003**, *63*, 1655−1661.
(41) Eslami, H.; Behrouz, M. Molecular dynamics simulation of a polyamide-66/carbon nanotube nanocomposite. *J. Phys. Chem. C* **2014**, *118*, 9841−9851.
(42) Pisani, W. A.; Wedgeworth, D. N.; Roth, M. R.; Newman, J. K.; Shukla, M. K. Computational prediction of mechanical properties of PA6−graphene/carbon nanotube nanocomposites. *J. Phys. Chem. C* **2021**, *125*, 15569−15578.
(43) Chiang, C.-R.; Chang, F.-C. Polymer blends of polyamide-6 (PA6) and poly (phenylene oxide)(PPO) compatibilized by styrene-maleic anhydride (SMA) copolymer. *Polymer* **1997**, *38*, 4807−4817.
(44) Hassan, A.; Othman, N.; Wahit, M. U.; Wei, L. J.; Rahmat, A. R.; Mohd Ishak, Z. A. Maleic anhydride polyethylene octene elastomer toughened polyamide 6/polypropylene nanocomposites: Mechanical and morphological properties. *Macromol. Symp.* **2006**, *239*, 182−191.
(45) Islam, K.; Saha, S.; Masud, A. Molecular dynamics simulation of the mechanical properties of CNT-polyoxymethylene composite with a reactive forcefield. *Mol. Simul.* **2020**, *46*, 380−387.
(46) Thompson, A. P.; Aktulga, H. M.; Berger, R.; Bolintineanu, D. S.; Brown, W. M.; Crozier, P. S.; in't Veld, P. J.; Kohlmeyer, A.; Moore, S. G.; Nguyen, T. D.; et al. LAMMPS - a flexible simulation tool for particle-based materials modeling at the atomic, meso, and continuum scales. *Comput. Phys. Commun.* **2022**, *271*, 108171.
(47) Van Duin, A. C.; Dasgupta, S.; Lorant, F.; Goddard, W. A. ReaxFF: a reactive force field for hydrocarbons. *J. Phys. Chem. A* **2001**, *105*, 9396−9409.
(48) Chenoweth, K.; Van Duin, A. C.; Goddard, W. A. ReaxFF reactive force field for molecular dynamics simulations of hydrocarbon oxidation. *J. Phys. Chem. A* **2008**, *112*, 1040−1053.
(49) Sharma, K.; Saxena, K. K.; Shukla, M. Effect of multiple Stone-Wales and Vacancy defects on the mechanical behavior of carbon nanotubes using Molecular Dynamics. *Procedia Eng.* **2012**, *38*, 3373−3380.
(50) Krishnan, A.; Dujardin, E.; Ebbesen, T.; Yianilos, P.; Treacy, M. Young's modulus of single-walled nanotubes. *Phys. Rev. B: Condens. Matter Mater. Phys.* **1998**, *58*, 14013−14019.
(51) Salvetat, J.-P.; Briggs, G. A. D.; Bonard, J.-M.; Bacsa, R. R.; Kulik, A. J.; Stöckli, T.; Burnham, N. A.; Forró, L. Elastic and shear moduli of single-walled carbon nanotube ropes. *Phys. Rev. Lett.* **1999**, *82*, 944−947.
(52) WenXing, B.; ChangChun, Z.; WanZhao, C. Simulation of Young's modulus of single-walled carbon nanotubes by molecular dynamics. *Phys. B* **2004**, *352*, 156−163.
(53) Lu, Q.; Bhattacharya, B. Effect of randomly occurring Stone−Wales defects on mechanical properties of carbon nanotubes using atomistic simulation. *Nanotechnology* **2005**, *16*, 555−566.
(54) Zhou, W.; Bai, X.; Wang, E.; Xie, S. Synthesis, structure, and properties of single-walled carbon nanotubes. *Adv. Mater.* **2009**, *21*, 4565−4583.
(55) Wang, H.; Li, Z.; Ghosh, K.; Maruyama, T.; Inoue, S.; Ando, Y. Synthesis of double-walled carbon nanotube films and their field emission properties. *Carbon* **2010**, *48*, 2882−2889.
(56) Arunkumar, T.; Karthikeyan, R.; Ram Subramani, R.; Viswanathan, K.; Anish, M. Synthesis and characterisation of multi-walled carbon nanotubes (MWCNTs). *Int. J. Ambient Energy* **2020**, *41*, 452−456.
(57) Shokrieh, M. M.; Rafiee, R. On the tensile behavior of an embedded carbon nanotube in polymer matrix with non-bonded interphase region. *Compos. Struct.* **2010**, *92*, 647−652.
(58) Chae, H. G.; Sreekumar, T.; Uchida, T.; Kumar, S. A comparison of reinforcement efficiency of various types of carbon nanotubes in polyacrylonitrile fiber. *Polymer* **2005**, *46*, 10925−10935.
(59) Niyogi, S.; Hamon, M.; Hu, H.; Zhao, B.; Bhowmik, P.; Sen, R.; Itkis, M.; Haddon, R. Chemistry of single-walled carbon nanotubes. *Acc. Chem. Res.* **2002**, *35*, 1105−1113.
(60) Mori, H.; Hirai, Y.; Ogata, S.; Akita, S.; Nakayama, Y. Chirality dependence of mechanical properties of single-walled carbon nanotubes under axial tensile strain. *Jpn. J. Appl. Phys.* **2005**, *44*, L1307.
(61) Natsuki, T.; Tantrakarn, K.; Endo, M. Effects of carbon nanotube structures on mechanical properties. *Appl. Phys. A: Mater. Sci. Process.* **2004**, *79*, 117−124.

https://doi.org/10.1021/acsaenm.4c00155
ACS Appl. Eng. Mater. 2024, 2, 1593−1602

(62) Humphrey, W.; Dalke, A.; Schulten, K. VMD: visual molecular dynamics. *J. Mol. Graphics* **1996**, *14*, 33−38.
(63) Plimpton, S. Fast parallel algorithms for short-range molecular dynamics. *J. Comput. Phys.* **1995**, *117*, 1−19.
(64) Dupont, V.; Germann, T. C. Strain rate and orientation dependencies of the strength of single crystalline copper under compression. *Phys. Rev. B: Condens. Matter Mater. Phys.* **2012**, *86*, 134111.
(65) Zheng, C.; Geng, F.; Rao, Z. Proton mobility and thermal conductivities of fuel cell polymer membranes: Molecular dynamics simulation. *Comput. Mater. Sci.* **2017**, *132*, 55−61.
(66) Chae, H. G.; Minus, M. L.; Kumar, S. Oriented and exfoliated single wall carbon nanotubes in polyacrylonitrile. *Polymer* **2006**, *47*, 3494−3504.
(67) Brown, A. M. A step-by-step guide to non-linear regression analysis of experimental data using a Microsoft Excel spreadsheet. *Comput. Methods Programs Biomed.* **2001**, *65*, 191−200.
(68) Stukowski, A. Visualization and analysis strategies for atomistic simulations. *Multiscale Materials Modeling for Nanomechanics*; Springer International Publishing, 2016; Vol. *245*, pp 317−336.
(69) Chen, H.-L.; Ju, S.-P.; Lin, K.-H.; Li, J.-Y.; Chen, H.-T. Investigation of mechanical properties and thermal stability of the thinnest tungsten nanowire by density functional theory. *RSC Adv.* **2016**, *6*, 1158−1168.
(70) Connolly, M. L. Computation of molecular volume. *J. Am. Chem. Soc.* **1985**, *107*, 1118−1124.

https://doi.org/10.1021/acsaenm.4c00155
ACS Appl. Eng. Mater. 2024, 2, 1593−1602